AAS 21-728

TWO-SPACECRAFT ORBITING IN OPPOSITION TO ENABLE BISTATIC RADAR OBSERVATIONS AROUND AN ASTEROID

Sonia Hernandez*, Saptarshi Bandyopadhyay*, Mark S. Haynes*, Reza R. Karimi*, and Rodney L. Anderson*

Fundamental answers about the origin and evolution of the Solar System hinge on our ability to image in detail the 3D interior structure of small bodies at high-resolution. By collecting radar measurements we can ultimately create 3D maps of the interior structure. In this study we focus our attention on a specific mission scenario which consists of a carrier spacecraft and two daughter spacecraft sent to orbit the asteroid Apophis. The orbits of the spacecraft are optimized to maximize radar measurements by dynamically modeling the harmonics and solar radiation pressure. For long mission durations, orbital correction maneuvers maintain the spacecraft in formation.

INTRODUCTION

Understanding the interior structure of solar system small bodies is critical for answering fundamental questions about the origin and evolution of the Solar System. Interior structure is also of vital importance for developing mitigation strategies for potentially-hazardous near-Earth asteroids (NEAs). Currently, the best known method for probing and imaging small body interiors is low-frequency radar (i.e,. 10-100 MHz).[1] Low-frequency radar can penetrate the interiors of both asteroids and comets while providing resolutions at the scale of 10s of meters. Simultaneous observations of radar reflections from multiple viewing angles and independent spacecraft can provide interior mapping analogous to medical CAT scans. For example, Figure 1 shows three spacecraft optimally transmitting and receiving radar data. The total coverage and diversity of viewing angles is critical to the ultimate image quality. The focus of this work is to identify candidate orbits for a bistatic radar system that needs to simultaneously observe a small body from different directions, with specific attention to ***antipodal***, or opposition, orbit configurations.

In general, there are three types of radar techniques for probing and investigating the interiors of small bodies:[2] 1) Tomographic synthetic aperture radar (SAR) that is used to create 3D images of volumetric backscatter,[3,4] 2) kinematic inversions of time-of-flight along ray paths to estimate the interior bulk dielectric,[5,6] and 3) full-wave nonlinear inverse scattering algorithms that create 3D interior maps of the dielectric constant via model-based inversion.[7–10] SAR images can be created in monostatic or bistatic configurations, while time-of-flight transmission measurements require bistatic radar on opposite sides of a small body, and inverse scattering algorithms benefit greatly from bistatic measurements (see Figure 2). In all cases, the greater the diversity of viewing angles, the better the image quality.

*Jet Propulsion Laboratory, California Institute of Technology, 4800 Oak Grove Drive, Pasadena, CA 91109. Corresponding Author: Sonia Hernandez; *Tel*: (818) 354-0418; *E-mail address*: Sonia.Hernandez-Doran@jpl.nasa.gov.

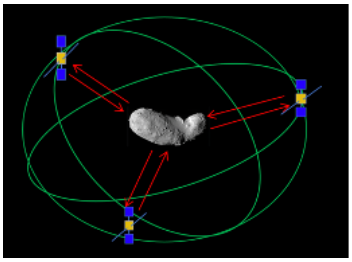

Figure 1. Multiple spacecraft orbiting a small body collecting monostatic and bistatic reflection and transmission measurements.

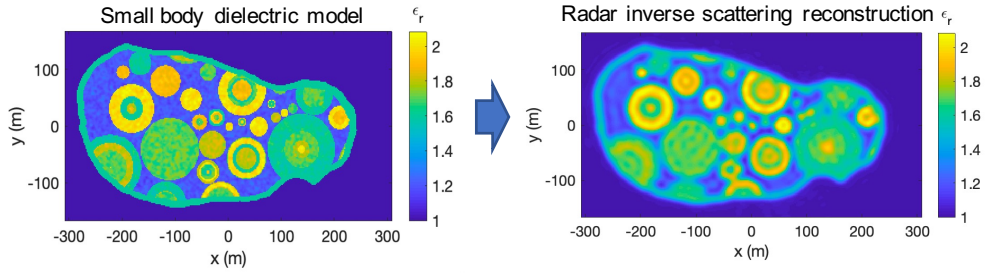

Figure 2. Example of 2D bistatic radar inverse scattering image of a small body interior dielectric model.[10] Left: true real part of the dielectric constant. Right: reconstructed dielectric constant under ideal acquisition conditions.

To date, only Rosetta-CONSERT has made limited bistatic transmission measurements of comet 67P/C-G,[11] which were made between the Rosetta spacecraft and the Philae lander. The average dielectric of the interior was estimated from the round-trip propagation time (method 2 above).[6] At present, ESA's Hera mission is being developed to investigate the asteroid Dydimos.[12] It will carry the CubeSat Juventas that will make a close investigation of the moon of the binary pair, Dydimos B (or Dydimoon). Juventas will carry the JuRa (Juventas Radar) instrument which will form 3D SAR images of the moon's interior.[13]

A possible future measurement configuration for a radar investigation of a small body, whether an asteroid or comet, envisions combining monostatic and bistatic radar measurements. Estimates of bulk dielectric properties from transmission measurements, together with high resolution 3D interior mapping, can together better address outstanding scientific hypotheses on interior structure, material heterogeneity, and bulk composition than either measurement alone. The spacecraft, instrument, and orbital design must then be designed to collect both monostatic and bistatic radar measurements.

Figure 3 shows how monostatic and bistatic radar measurements can be sub-divided into four broad categories:

- **Monostatic :** A spacecraft transmits a radar signal towards the small body, and then measures the reflected radar signal from the small body. No coordination between multiple spacecraft is necessary for monostatic measurements.

- **Antipodal (or opposition):** A spacecraft transmits a radar signal towards the small body, and a different spacecraft measures the radar signal that has traveled through the small body. Here the transmitting and receiving spacecraft must maintain diametrically opposite positions.

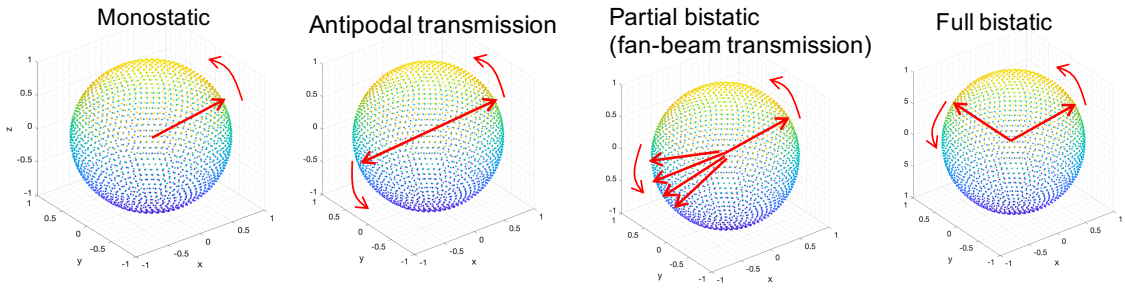

Figure 3. Types of radar measurements.

- **Partial bistatic :** Like the antipodal configuration, two radar systems capture transmission, or near-grazing, measurements through the small body. Here the transmitting and receiving spacecraft must maintain opposite positions, but with looser constraints that pure antipodal.
- **Full bistatic :** A large diversity of bistatic radar echoes are measured with the goal of collecting as many as possible given mission time and resource constraints. Depending on coverage requirements, significant coordination between multiple spacecraft may be necessary.

The ultimate goal of this study is to help answer the following questions: Can the orbits of a swarm of spacecraft be designed to complete the coverage requirements for small body bistatic radar tomography? How long does it take to achieve maximum coverage? Is reconfiguration of the swarm necessary to achieve the science objective? These are broad questions, so in this preliminary study we focus our attention on monostatic and antipodal radar measurements only. As a sample mission architecture, consider a carrier spacecraft that rendezvouses with a small body and releases two small satellites (smallSats). The two smallSats use propulsive maneuvers to disperse around the body in perfect antipodal configuration, as illustrated in Figure 4. To map the interior structure, either a) the carrier spacecraft transmits a radar signal, which travels through the small body and is received by the two daughter spacecraft, or b) all spacecraft transmit radar signals to be received by the other spacecraft. In order to accomplish complete coverage of bistatic radar measurements around the small body, 10,000s to 100,000s of echoes need to be recorded.

In this paper we focus on designing the orbits of the two smallSats such that they remain in antipodal configuration by sweeping through a range of initial conditions, including orbital altitude around the small body. The optimal initial conditions are then used to determine how long it takes to complete the coverage requirement using bistatic radar observations. Due to the highly perturbed environment around small bodies (higher order harmonics, solar radiation pressure, etc.), the spacecraft will fall off perfect opposition after some period of time, and will need to be reconfigured by using propulsive maneuvers. Even though our algorithms are general for any small body, the results in this paper focus around the asteroid (99942) Apophis. Apophis will perform a close approach with our planet at 38,000 km on April 13th 2029. Apophis is a potentially hazardous asteroid and understanding its interior structure via radar measurements may be critical for future deflection or mitigation strategies.

The paper is organized as follows. The next section discusses the spacecraft dynamical model and the method used to obtain the harmonics of Apophis based on a preliminary shape model. In the

following section we determine the best orbital initial conditions to maintain antipodal configuration for a range of orbiting altitudes. Once the initial conditions of the two daughter spacecraft are chosen, radar positions are modeled to determine how long is needed to completely map the asteroid, which is outlined in the next section. We discuss how solar radiation pressure affects the stability of the orbits, and in the final section, we discuss conclusions and future work.

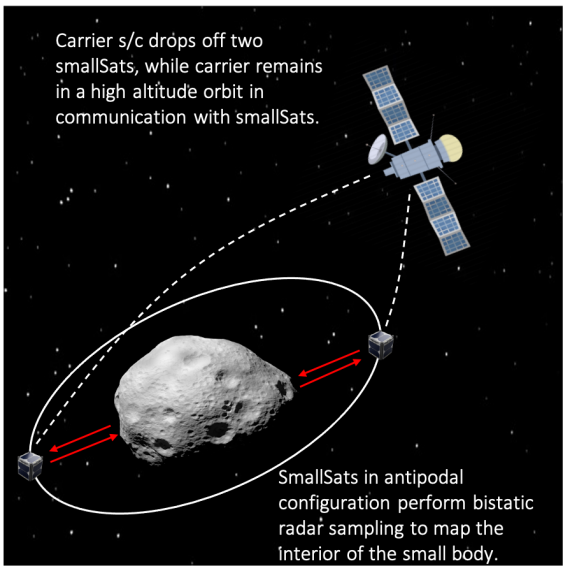

Figure 4. Mission schematic: Carrier spacecraft drops off two smallSats into antipodal configuration. The smallSats will perform bistatic radar sampling to map the interior of the small body.

SPACECRAFT DYNAMICAL MODEL

The dynamics of a spacecraft around a minor body are dominated by different type of forces. These forces can be modeled at different levels of fidelity, as shown in Figure 5. The simplest model is represented by a single point mass, in which the model of the minor body is assumed to be spherical in shape (1). Adding spherical harmonics or polyhedral mass models to the gravity of the minor body increases fidelity by adding a more realistic gravitational shape to the body (2). Finally, one can add other non-gravitational forces, such as solar radiation pressure (SRP), which is of particular importance to spacecraft orbiting minor bodies (3).

The equations of motion of a spacecraft around a small body are

$$\ddot{\mathbf{r}}_i = -\frac{\mu}{||\mathbf{r}_i||^3}\mathbf{r}_i + \frac{\partial R}{\partial \mathbf{r}_i} + \mathbf{a}_{SRP_i} + \mathbf{a}_{\Delta V_i} + \mathbf{a}_{other} \tag{1}$$

where $\mathbf{r}_i$ is the position vector of spacecraft i with respect to the small body, μ is the gravitational parameter of the small body, and R is the potential of a higher order gravity field (see References 14 and 15). The VW-method outlined by Montenbruck and Gill[16] is implemented here to compute the the higher degree order acceleration, and its explanation is omitted from this paper. The acceleration due to solar radiation pressure ($\mathbf{a}_{SRP_i}$) is simplified as

$$\mathbf{a}_{SRP_i} = \frac{P_{SRP} C_R A_i}{m_{sc_i}} \hat{\mathbf{s}}_i \tag{2}$$

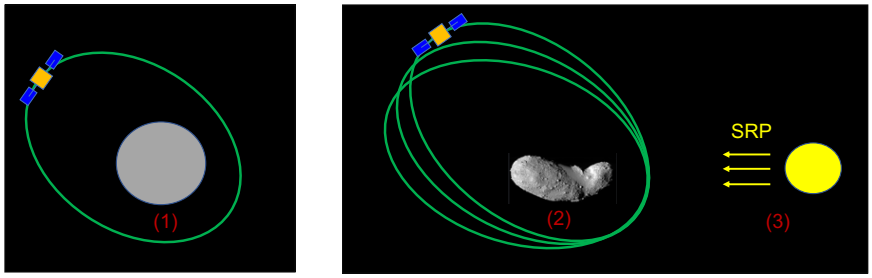

Figure 5. Forces acting on a spacecraft orbiting a minor body can be modeled with different levels of fidelity. (1) is the simplest model and assumes spherical model for the small body; one can increase complexity by adding spherical harmonics to the minor body (2) and solar radiation pressure (3).

where $\hat{\mathbf{s}}_i$ is in the direction of the Sun-spacecraft vector, P_{SRP} is solar pressure, C_R is the coefficient of reflectivity, A_i is the incident surface area, and m_{sc_i} is the mass of spacecraft i. The acceleration due to maneuvers, $\mathbf{a}_{\Delta V_i}$, is only used when controlling or reconfiguring the spacecraft. Lastly, the term $\mathbf{a}_{other}$ represents any other perturbations acting on the spacecraft, including solar tides and gravitational perturbations coming from other bodies. This last term is in general small and is not included in the results of this paper.

Apophis Shape Model

This section briefly explains the generation of Apophis' shape and gravity model. Apophis shape model was obtained using radio Doppler measurements[17] and was provided to us by the JPL Solar System Dynamics Group in the form of polyhedrons. SBDT (Small Body Dynamic Toolkit), a JPL in-house tool, was then used to convert the polyhedron shape model, provided a given homogenous density, into Apophis's gravity model (see Figure 6).

The assumption on density is important in generating the gravity model for a small body. For SBDT the density of the small body can be either 1) computed from the volume (known from the shape model) and μ (if it is well known from radio science observations), or 2) chosen based on the best assumption from on empirical data. For example, Itokawa's density based on radio science measurements has been computed as 1.98567 gr/cm^3. Therefore, for near-Earth objects for which we have no gravitational data, choosing a density of 2 gr/cm^3 is in general a very good initial guess. For Apophis, based on the suggestion from the Solar System Dynamic Group, we assume a density of 2 gr/cm^3 since its accurate estimated μ is not currently available. The order (n) and degree of Legendre Polynomials (m) generates in SBDT an nxm spherical harmonics gravity model. For this study, we used up to an 8x8 gravity model; the spherical harmonic coefficients are listed in the Appendix. The mean radius of Apophis is

$$R_{Apophis} = 0.2224\ km$$

and the gravitational mass parameter

$$\mu = 2.64595 \cdot 10^{-9}\ km^3/s^2.$$

MISSION DESIGN OF TWO SPACECRAFT IN ANTIPODAL CONFIGURATION

In order to take antipodal transmission measurements we require that two spacecraft be opposite of each other ($180^o +/- \Delta$) at any point in time, where Δ is the deviation from the center line

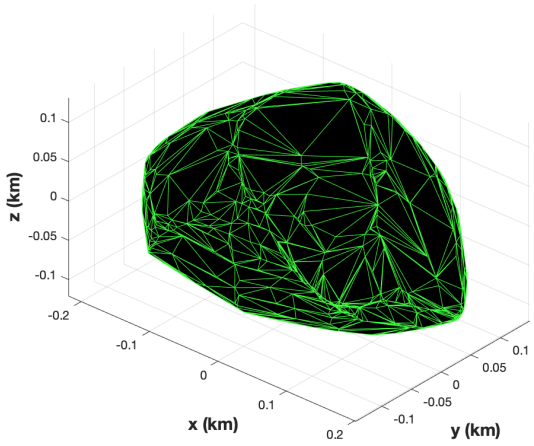

Figure 6. Apophis' Shape Model.

through the object. If only a point mass model is assumed, then clearly any set of initial conditions in which the two spacecraft are in the same circular orbit with a 180^o offset will attain antipodal coverage. In this case, the orbital elements of both spacecraft are the same, other than the true anomaly, where $\nu_2 = \nu_1 + 180^o$. Once other gravitational forces, such as higher order harmonics, are introduced in the model, the perturbations will be significant, and no set of initial conditions will result in antipodal coverage.

Figure 7 shows an example of two spacecraft orbiting Apophis at an initial radius of $3R_{Apophis}$ for a total of 30 days. The eccentricity and inclination are set to $e = 0$ and $i = 45^o$ for this example, respectively. The trajectory propagated with 4^{th} order degree harmonics is shown in (a), whereas the angle between both spacecraft over time is shown in blue in (b). If only a point mass model were used, then the spacecraft would not precess and they would remain at 180^o from each other (red line in (b)). Notice how the two spacecraft begin at 180^o from each other, by design, but due to the nonlinearities in the dynamics of the asteroid, the trajectories become perturbed and exact antipodal geometry cannot be maintained. Both spacecraft must move around Apophis in similar orbits, but opposite of each other. The goal is to *choose the optimal initial conditions* of both spacecraft such that they maintain a geometry as close as possible to 180^o for the mission duration, therefore maximizing antipodal coverage.

In Figure 8 we can visualize just how critical it is to choose the right initial conditions for both spacecraft in the swarm. Assuming two spacecraft in initial circular orbits, with a radius of $3R_{Apophis}$, and inclination of $90°$, we vary the right ascension of ascending node (precession in the orbit) and the initial true anomaly of the first spacecraft (ν_1). Note, $\nu_2 = \nu_1 + 180°$. We record the percentage of time that both spacecraft are in antipodal configuration ($180^o +/- \Delta$), where Δ depends on the specific science requirements (varies as $\Delta = [2, 5, 10, 20]^o$) and the total simulation time is 20 days. There are optimal regions of initial conditions where antipodal configuration is met all the time (yellow contour), and regions where the orbits are extremely perturbed and antipodal configuration is met less than 10% of the time (blue contour). Of course, there is a trade-off between how large the angle Δ can be while still being able to take the desired radar measurements.

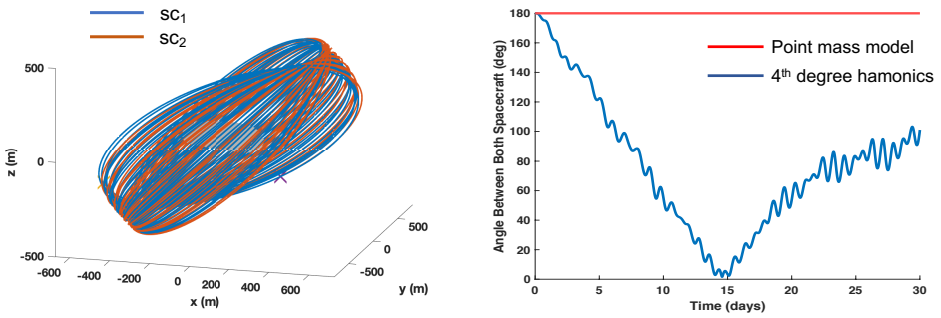

(a) Trajectory (b) Angle between spacecraft as a function of time.

Figure 7. Two spacecraft orbiting Apophis at a radius of $3R_{Apophis}$ for a simulation time of 30 days. The spacecraft are not in antipodal configuration when including higher order harmonics.

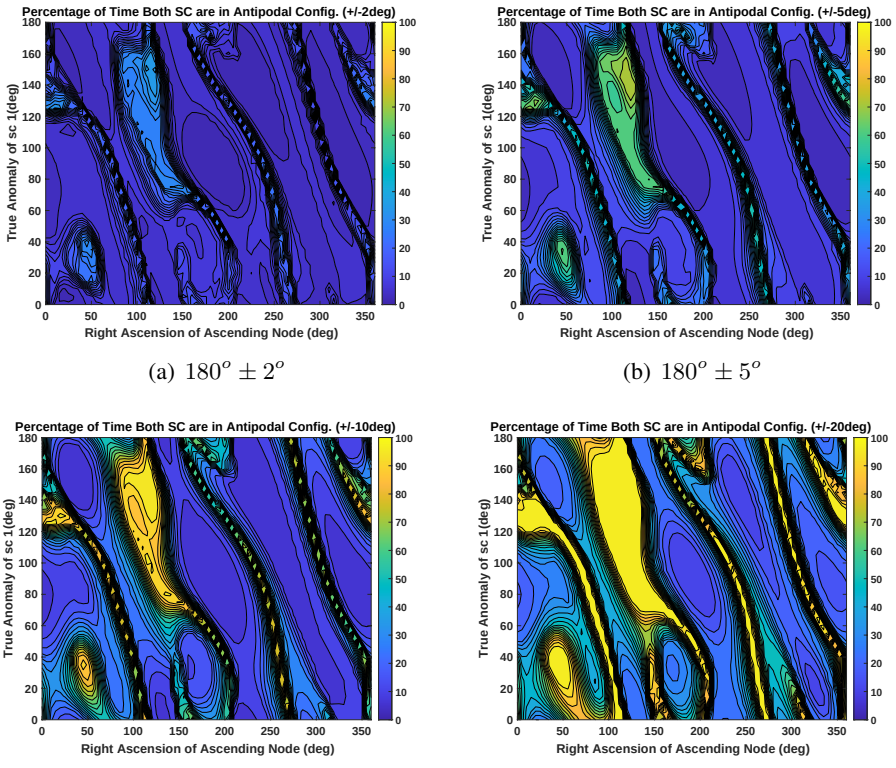

(a) $180^o \pm 2^o$ (b) $180^o \pm 5^o$

(c) $180^o \pm 10^o$ (d) $180^o \pm 20^o$

Figure 8. Contour plots of percentage of time that both spacecraft are in antipodal configuration for a 20 day mission simulation, for orbits at a semi-major axis $a = 3R_{Apophis}$.

Using the contour plot in Figure 8(c), one can choose the following set of initial orbital elements to maintain antipodal coverage: $a = 3R_{Apophis}$, $e = 0$, $i = 90^o$, $\omega = 0^o$, $\Omega = 115^o$, $\nu_1(t_0) = 150^o$ and $\nu_2(t_0) = 330^o$, where ω is the argument of periapsis (not defined for circular orbits, hence set to zero) and Ω is the right ascension of ascending node. The trajectory and angle between both

spacecraft over time for this set of initial orbital elements is shown in Figure 9. The angle between both spacecraft in Figure 9(b) wobbles around $180^o \pm 10^o$, but is in a fairly stable region. The beam or limb angle is defined in Figure 10, and represents the maximum angle at which two opposing radar instruments are considered to be in a transmission configuration.

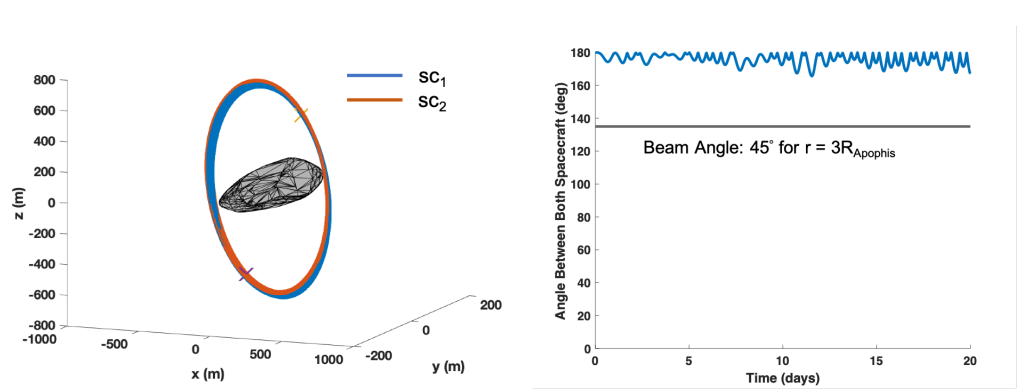

(a) Trajectory

(b) Angle between both spacecraft as a function of time.

Figure 9. Two spacecraft orbiting Apophis at an altitude of $3R_{Apophis}$ for a simulation time of 20 days.

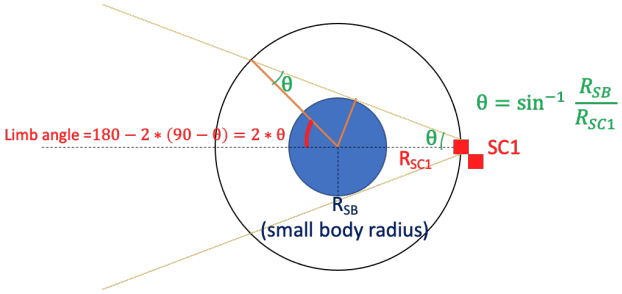

Figure 10. Limb angle of a spacecraft with respect to 180^o line.

In the example in Figure 8(a), maintaining a tight antipodal configuration ($180^o +/- 2^o$) while orbiting at a semi-major axis $a = 3R_{Apophis}$ is impossible, since regardless of the set of initial conditions the antipodal requirement will be met at most 30% of the simulation time. However, once the antipodal requirement can be loosened to ($180^o +/- 10^o$) as in Figure 8(c), a few options begin to appear where the spacecraft will remain in antipodal configuration for 20 days without the need for stationkeeping. Note, this is assuming perfect knowledge of the harmonics of the asteroid and does not take into account any uncertainties in the gravitational model. If the spacecraft increase their orbiting altitude, the spherical harmonic values become less dominant, and orbits are more stable. Figure 11 shows contours of percentage of time in antipodal configuration for a set of initial circular orbits at $a = 5R_{Apophis}$ and $i = 90^o$. At this orbiting altitude, the antipodal requirement can be much tighter, since Figure 11(a) with a $\Delta = 2^o$ offers stable bands of initial conditions that will retain the spacecraft in opposition. As the Δ requirement is relaxed, these stable bands open up, up to the point where any set of initial conditions chosen will ensure antipodal coverage (Figure 11(d)).

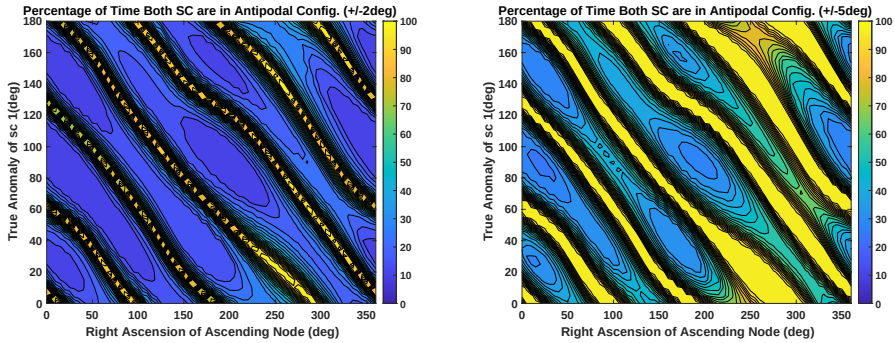

(a) $180^o \pm 2^o$ (b) $180^o \pm 5^o$

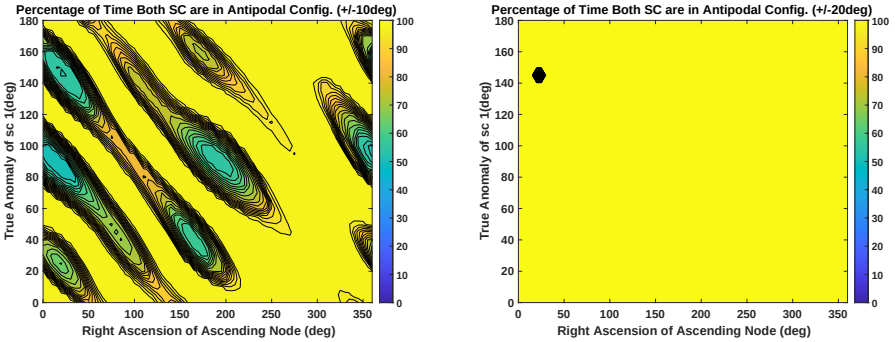

(c) $180^o \pm 10^o$ (d) $180^o \pm 20^o$

Figure 11. Contour plots of percentage of time that both spacecraft are in antipodal configuration for a 20 day mission simulation, for orbits at a semi-major axis $a = 5R_{Apophis}$**.**

The variation in parameters such as Δ and the orbiting altitude and inclination changes the amount of time the spacecraft are in opposition. Table 1 shows the percentage of time two spacecraft orbiting at an initial $e = 0$ and $i = 90^o$ are in opposition ($180^o \pm \Delta$) for different values of semi-major axis, assuming 4^{th} order spherical harmonic coefficients and no SRP. At $a = 2R_{Apophis}$ there is no single set of initial conditions that can result in two spacecraft remaining in opposition for a 20 day mission simulation. At this radius, the non-spherical gravity from the small body is very strong. As the altitude is increased, several options of initial conditions begin to appear. Once the spacecraft are orbiting at $a = 5R_{Apophis}$, even the most stringent antipodal requirement can be met by choosing the right initial conditions.

Table 1. Percentage of time two spacecraft orbiting at an initial $e = 0$ **and** $i = 90^o$ **are in opposition** ($180^o \pm \Delta$) **for different values of semi-major axis.**

Semi-Major Axis	2R$_{Apophis}$	3R$_{Apophis}$	4R$_{Apophis}$	5R$_{Apophis}$	8R$_{Apophis}$
$180^o \pm 2^o$	6%	40 %	78 %	100 %	100%
$180^o \pm 5^o$	11%	75 %	100 %	100 %	100%
$180^o \pm 10^o$	21%	99 %	100 %	100 %	100%
$180^o \pm 20^o$	33%	100 %	100 %	100 %	100%
$180^o \pm$ limb angle	69%	100 %	100 %	100 %	100%

The variation in parameters such as Δ and the orbiting altitude and inclination changes the amount

of time required to complete coverage of the asteroid for the different types of radar transmission. The inclination in the contour plots presented in this section are set to 90^o as they offer the most stable solutions and maximum observation coverage (the poles can only be observed if orbiting in a polar orbit). The next section outlines the computation of the radar coverage metric.

Orbit Inclination and Stability

The previous simulations showed contour solutions for 90° inclination orbits only. Polar orbits were baselined because they are the only ones capable of taking measurements of the the entire small body, including the poles. In this subsection we investigate the stability of lower inclination orbits, with the caveat that observation of the entire body might not be achievable. Figure 12 shows contour plots of percentage of time in antipodal configuration for two spacecraft at an initial altitude of $2R_{Apophis}$ (semi-major axis of $3R_{Apophis}$), eccentricity zero, and varying inclination (subfigures (a)–(f)). As can be observed, the higher inclination solutions have more stable regions, where antipodal configuration can be met for the simulation period time. Lower inclination solutions have few to zero solutions in antipodal configuration 100% of the time (yellow contours). Therefore, from a stability point of view as well as a science observation point of view, polar orbits are best for this kind of application.

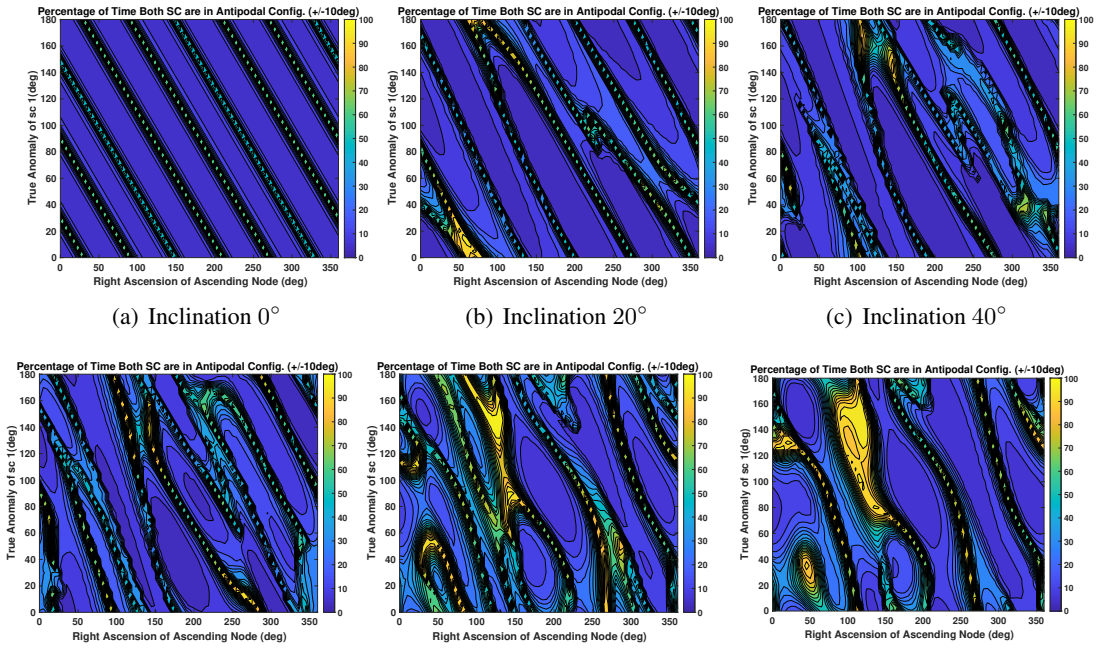

(a) Inclination 0° (b) Inclination 20° (c) Inclination 40°

(d) Inclination 60° (e) Inclination 80° (f) Inclination 90°

Figure 12. Contour plots of percentage of time that both spacecraft are in antipodal configuration for a 20 day mission simulation, for orbits at a semi-major axis $a = 3R_{Apophis}$ with varying inclination.

MAXIMIZING RADAR OBERSVATIONS

In order to perform monostatic radar observations, the spacecraft has to make multiple measurements of the small body. The maximum angular step ($\Delta\theta$) between adjacent sampling positions is

given by:[18]

$$\Delta\theta \leq \frac{1}{4}\frac{\lambda}{r_{\mathrm{SB}}}\,, \tag{3}$$

where λ is the radar wavelength and r_{SB} is the radius of the small body. The total number of sampling points is given by:[18]

$$N = \frac{4\pi}{\Delta\Omega}\,, \tag{4}$$

$$\text{where } \Delta\Omega \approx \pi\left(\frac{\Delta\theta}{2}\right)^2\,, \tag{5}$$

where $\Delta\Omega$ is the solid angle of the local region covered by each sampling measurement. Figure 13 shows the total number of sampling points necessary for monostatic radar observations as a function of radar's operating frequency and small body diameter. For example, if to perform 60 MHz frequency (5 m wavelength) monostatic radar observations of a small body such as Apophis, then we need approximately $5 \cdot 10^5$ sampling points to collect all the necessary science data. The lower the operating frequency, the lower the number of sampled points required.

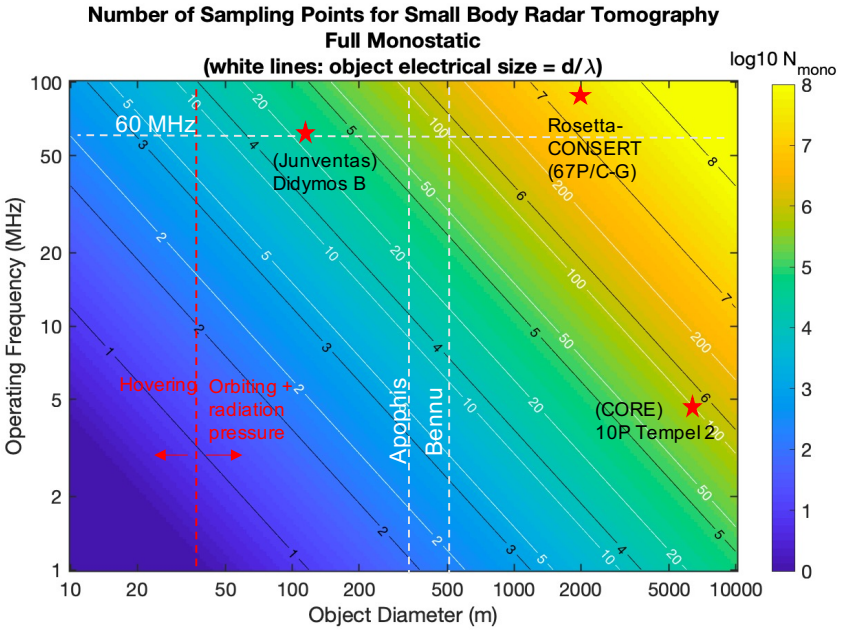

Figure 13. Number of sampling points as a function of radar frequency and small body diameter.

In this study, we assume that antipodal radar observations have the same maximum angular step as monostatic radar observations, hence they also need the same total number of sampling points N in Eq. (4) and Figure 13. Bistatic radar observations on the other hand need a lot more sampling points. For each location of the transmitting spacecraft, there are N in Eq. (4) locations for the receiving spacecraft. Hence the total number of sampling points is $N \times N$.

Measurement models for Radar Observations

In this subsection we describe when a spacecraft performs a radar measurement. Recall, $\mathbf{r}_i(t)$ represents the position of the i^{th} spacecraft at time t with respect to the small body in the inertial

reference frame. Let $\mathbf{p}_j(t)$ represent the position of the j^{th} sampling point at time t in the inertial reference frame. Note that the sampling points do not move with respect to the small body, i.e. they are invariant in the small body fixed reference frame. The measurement models are as follows:

- **Monostatic :** The i^{th} spacecraft makes a valid monostatic radar measurement at the j^{th} sampling point at time t, when it is within $\frac{\Delta\theta}{2}$ angular distance from that sampling point, i.e.:

$$\cos^{-1}\left(\frac{\mathbf{r}_i(t)}{\|\mathbf{r}_i(t)\|_2}\cdot\frac{\mathbf{p}_j(t)}{\|\mathbf{p}_j(t)\|_2}\right)\leq\frac{\Delta\theta}{2}\,, \tag{6}$$

  where $\Delta\theta$ is defined in Eq. (3).

- **Antipodal :** In addition to the monstatic constraint in Eq. (6), we need another spacecraft that is diametrically opposite from the i^{th} spacecraft to measure the radar signal that has traveled through the small body. Let $\mathbf{r}_\ell(t)$ represent the position of the ℓ^{th} spacecraft at time t in the inertial reference frame.

  For an antipodal threshold angle of Θ deg, the i^{th} transmitting spacecraft and the ℓ^{th} receiving spacecraft makes a valid antipodal radar measurement at the j^{th} sampling point at time t, if:

$$\cos^{-1}\left(\frac{\mathbf{r}_i(t)}{\|\mathbf{r}_i(t)\|_2}\cdot\frac{\mathbf{p}_j(t)}{\|\mathbf{p}_j(t)\|_2}\right)\leq\frac{\Delta\theta}{2}\,, \tag{7}$$

$$\cos^{-1}\left(\frac{\mathbf{r}_i(t)}{\|\mathbf{r}_i(t)\|_2}\cdot\frac{\mathbf{r}_\ell(t)}{\|\mathbf{r}_\ell(t)\|_2}\right)\geq 2\pi-\Theta\,, \tag{8}$$

- **Bistatic :** Here there is no constraint on the position of the receiving spacecraft. Let $\mathbf{p}_k(t)$ represent the position of the k^{th} sampling point at time t in the inertial reference frame.

  The i^{th} transmitting spacecraft and the ℓ^{th} receiving spacecraft makes a valid bistatic radar measurement at the (j,k) sampling points pair at time t, if:

$$\cos^{-1}\left(\frac{\mathbf{r}_i(t)}{\|\mathbf{r}_i(t)\|_2}\cdot\frac{\mathbf{p}_j(t)}{\|\mathbf{p}_j(t)\|_2}\right)\leq\frac{\Delta\theta}{2}\,, \tag{9}$$

$$\cos^{-1}\left(\frac{\mathbf{r}_\ell(t)}{\|\mathbf{r}_\ell(t)\|_2}\cdot\frac{\mathbf{p}_k(t)}{\|\mathbf{p}_k(t)\|_2}\right)\leq\frac{\Delta\theta}{2}\,, \tag{10}$$

Orbits for Maximizing Radar Observations

We now compute the percentage of body observed over a 20 day simulated mission assuming 10^4 sampled points for different sets of orbital initial conditions. For a semi-major axis of $3R_{Apophis}$, eccentricity of zero, and polar inclination, we sweep through the right ascension of ascending node and true anomaly of one spacecraft at the initial epoch, in the same fashion as before. Figure 14(a) shows the amount of time in antipodal configuration (replicating the results in 14), while 14(b) shows the percentage of body observed in the same amount of time. The subfigures from left to right vary from $180^o \pm 2^o$ (leftmost subfigure) to $180^o \pm 20^o$ (rightmost subfigure). The red dot in each subfigure represents the optimal location to maximize observations. After 20 days, the optimal antipodal configuration yields approximately 80% of the body observed.

Figure 15 shows similar results for spacecraft orbiting at a semi-major axis of $5R_{Apophis}$ and with only 5,000 sampled points. This would correspond to a radar with an operating between 5-10 MHz.

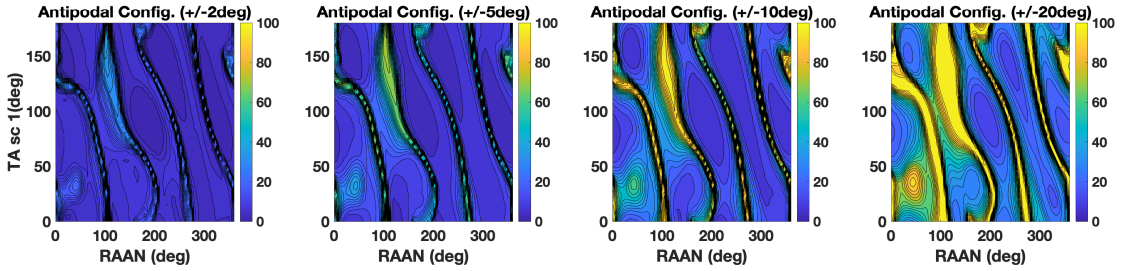

(a) Percentage of Time in Antipodal Configuration

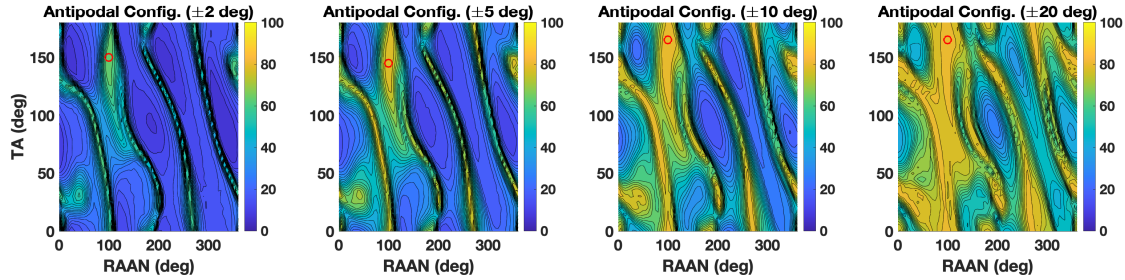

(b) Percentage of Body Observed

Figure 14. Contour plots representing the optimal initial conditions for two spacecraft in antipodal configuration at a radii of $3R_{Apophis}$ with 10,000 sampled points.

Even though there are many stable solutions that yield antipodal configuration for 100% of the 20 day simulation (yellow contours in (a)), only 80% of the body can be observed in that amount of time (orange contours in (b)). Table 2 summarizes the amount of body observed after 20 days for different orbiting radii and antipodal requirement, assuming 5,000 simulated points. Each solution represents the optimal set of initial conditions that yields the maximum amount of time in antipodal configuration. Even though solutions become more stable as orbital altitude increases (as indicated by Table 1), the slow rotation of the orbits yields less percentage observed of the body for the same amount of time than orbits at a higher altitude. The optimal orbiting radius that maximizes both stability to maintain antipodal configuration and percentage of body observed in the least amount of time is $3R_{Apophis}$ with an antipodal requirement of $180^o \pm 10^o$. For these conditions, we maintain antipodal configuration for 99% of the time (Table 1) and observe 97% of the body (Table 2).

Table 2. Maximum percentage of body observed after a 20 day simulation with 5000 simulated points, at an initial $e = 0$ and $i = 90^o$ for different values of semi-major axis.

Semi-Major Axis	2R$_{Apophis}$	3R$_{Apophis}$	4R$_{Apophis}$	5R$_{Apophis}$	8R$_{Apophis}$	10R$_{Apophis}$
$180^o \pm 1^o$	7%	30%	32%	30%	28%	28%
$180^o \pm 2^o$	20%	83%	85%	80%	74%	72%
$180^o \pm 5^o$	33%	96%	91%	87%	77%	76%
$180^o \pm 10^o$	46%	97%	92%	87%	77%	76%
$180^o \pm 20^o$	61%	98%	92%	87%	77%	76%
$180^o \pm$ limb angle	83%	98%	92%	87%	77%	76%

Antipodal radar observation for different number of sampling points, ranging from $1,000$ to $500,000$, and antipodal threshold angle of $\theta = 10$ degrees are shown in Figure 16. The semi-major axis (SMA) of the spacecraft orbits range from 2 to 10 small body radii. The initial conditions

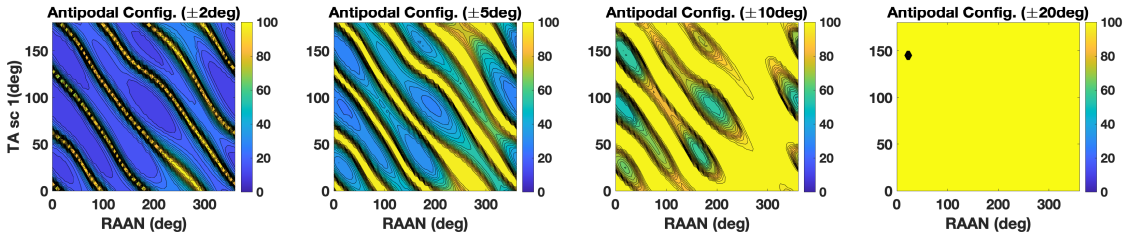

(a) Percentage of Time in Antipodal Configuration

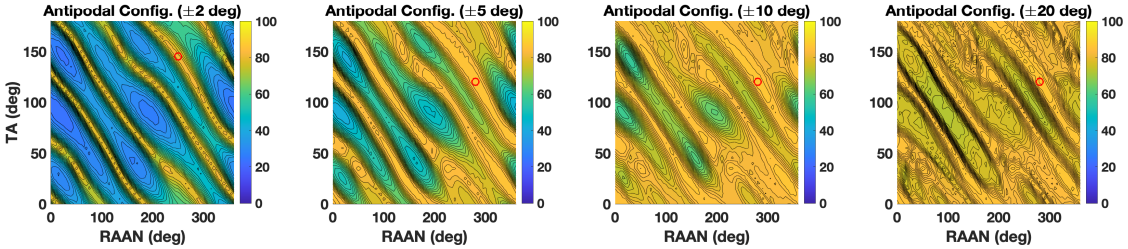

(b) Percentage of Body Observed

Figure 15. Contour plots representing the optimal initial conditions for two spacecraft in antipodal configuration at a radii of $5R_{Apophis}$ with 5,000 sampled points.

Semi-Major Axis (SMA)	**Right Ascension of Ascending Node (RAAN)**	**True Anomaly (TA) of s/c 1 at t_0**
2×Radius	340°	90°
3×Radius	105°	145°
4×Radius	40°	145°
5×Radius	280°	120°
6×Radius	65°	95°
7×Radius	345°	130°
8×Radius	240°	10°
9×Radius	85°	90°
10×Radius	30°	130°

Table 3. Initial conditions for the simulation results shown in Figure 16.

used for each simulation are in Table 3 with zero eccentricity and 90^o inclination common to all solutions. These initial conditions are chosen as the optimal from the contour plots in the previous section. Note that some orbits are unable to collect all the data due to orbital resonances. For the simulation of a semi-major axis of $3R_{Apophis}$ (red curve), it is apparent that for low number of sampled points, the entire body can be observed in a short amount of time (e.g., less than two months for $1e4$ sampled points). However, as sample points increase, the amount of time required to observe the entire body increases as well, in an asymptotic behavior (e.g., one year to observe Apophis using $5e5$ sampled points). Since number of sampled points required for a mission is a direct function of radar operating frequency, choosing the right type of radar is key for such a mission.

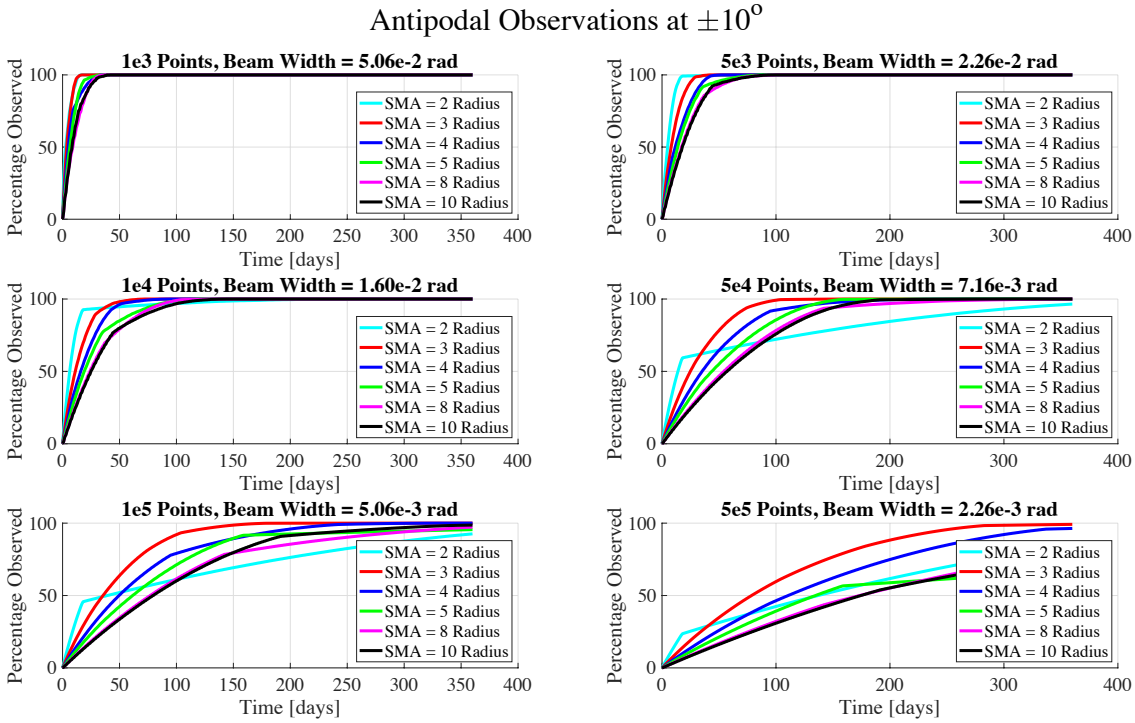

Figure 16. Antipodal radar observation times around Apophis, with antipodal threshold angle of $\theta = 10$ deg.

SOLAR RADIATION PRESSURE

The simulations shown up to now only include up to 4^{th} order harmonics of the body. In this section, we briefly discuss how the results change when adding higher order harmonics and SRP. We assume both spacecraft in antipodal configuration are small 6U CubeSats, with 14 kg of mass each. Figure 17 compares contour plots that show percentage of time in antipodal configuration for polar orbits at a semi-major axis of $3R_{Apophis}$, eccentricity of zero, and varying right ascension of ascending node and true anomaly, for different levels of fidelity, assuming antipodal requirement of $180^o \pm 10^o$. Figure 17(a) shows the results assuming only 4^{th} order harmonics (equivalent to Figure 8(c)), 17(b) increases fidelity to 8^{th} order, and lastly 17(c) includes SRP. The yellow contours represent 100% of the time in antipodal configuration. As expected, when SRP is added, most stable solutions disappear, although there are still a few regions of stability. Choosing the most optimal solution with SRP, the maximum time in antipodal observation drops to 84% after 20 days, as can be seen in Figure 18.

CONCLUSION AND FUTURE WORK

In this paper we explore optimal orbit configuration for two spacecraft orbiting a small body with the goal of taking transmission bistatic radar measurements. For two spacecraft to do so, they must remain in opposition the majority of the mission lifetime. Perturbations in the spacecraft dynamics play a large role in determining whether two spacecraft will remain in antipodal configuration and for how long. For an example case of spacecraft orbiting Apophis, we show that, at an orbiting

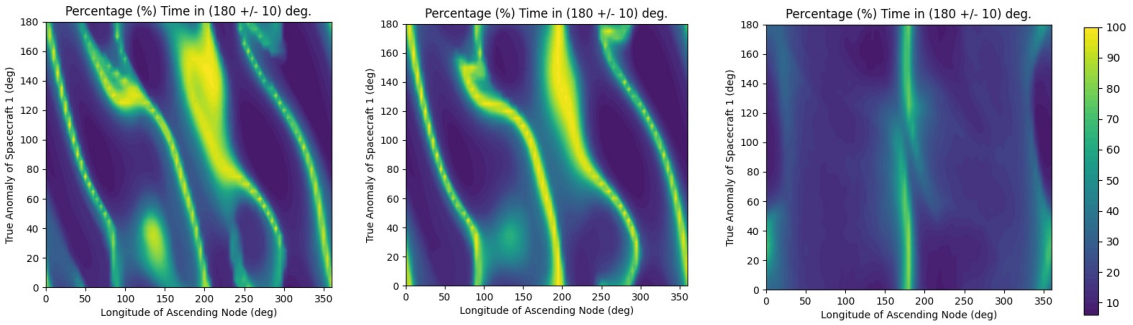

(a) 4^{th} Order Harmonics (b) 4^{th} Order Harmonics (c) 8^{th} Order Harmonics + SRP (d)

Figure 17. Contour plots of percentage of time that both spacecraft are in antipodal configuration for a 20 day mission simulation, for orbits at a semi-major axis $a = 3R_{Apophis}$, with an antipodal requirement of $180^o \pm 10^o$, for varying levels of dynamic fidelity.

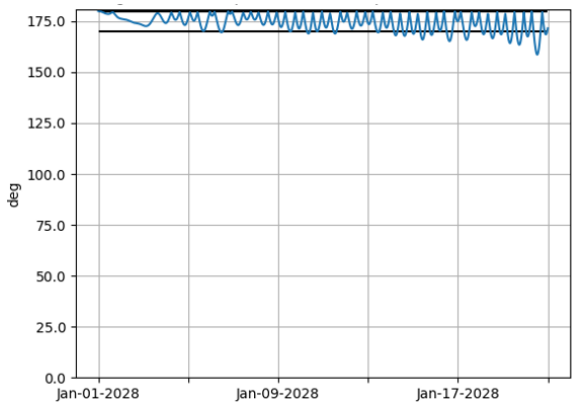

Figure 18. Angle between two spacecraft over a 20 day simulation, choosing the optimal initial conditions in Figure 17(c). These results include 8^{th} order harmonics and SRP.

radius or $3R_{smallbody}$, antipodal configuration can be met if the requirement is relaxed to $180^o \pm 10^o$. At an orbiting radius of $5R_{smallbody}$, the requirement can be much more stringent, and antipodal configuration can be met $180^o \pm 2^o$. Solar radiation pressure adds a big factor in the stability of the results.

In future work we plan to incorporate uncertainties in our models to see how large the dynamical perturbations may be, and design stationkeeping maneuvers to maintain the formation in antipodal configuration. We estimate ΔV costs to transfer the daughter spacecraft from their carrier spacecraft into their respective science orbits. We also plan to increase the number of daughter spacecraft to determine how much faster bistatic radar measurements can be taken to completely map out the small body. Using this insight into the coverage trade space, mission architects will be able to select the appropriate number of daughter spacecraft, observation strategies, and other key aspects for future mission development to characterize the interior of primitive bodies in the Solar System.

APPENDIX: SPHERICAL HARMONIC COEFFICIENTS OF APOPHIS

The spherical harmonic coefficients for Apophis up to degree and order 8 are listed in Table 4 and 5. Note, the *zonal* harmonics $J_l = -C_{l,0}$. In Table 5, the $C_{l,m}$ and $S_{l,m}$ coefficients are referred to as *tesseral* harmonics if $l \neq m$ and as *sectoral* harmonics if $l = m$.[19]

Table 4. Zonal harmonic coefficients.

J_1	0.00000e+00
J_2	1.99783e-02
J_3	−7.54020e-03
J_4	−5.10541e-04
J_5	1.00249e-03
J_6	−3.56025e-04
J_7	−7.56042e-05
J_8	−3.47789e-05

ACKNOWLEDGMENT

Special thanks to Marina Brozovic for providing the Apophis shape model. This research was carried out at the Jet Propulsion Laboratory, California Institute of Technology, under a contract with the National Aeronautics and Space Administration.

© 2021. California Institute of Technology. Government sponsorship acknowledged.

REFERENCES

[1] M. Haynes, A. Virkki, F. Venditti, D. Hickson, N. Pinilla-Alonso, J. Brisset, L. Benner, C. Raymond, J. Lazio, A. Freeman, *et al.*, "Asteroids Inside Out: Radar Tomography, Community White Paper for the Planetary Decadal Survey, 2023-2032," 2020.

[2] A. Safaeinili, S. Gulkis, M. Hofstadter, and R. Jordan, "Probing the interior of asteroids and comets using radio reflection tomography," *Meteoritics & Planetary Science*, Vol. 37, No. 12, 2002, pp. 1953–1963.

[3] Y. Gim, E. Heggy, D. Arumugam, X. Wu, and E. I. Asphaug, "3D Synthetic Aperture Radar Imaging of the Interior of the Cometary Nucleus," *AGUFM*, Vol. 2014, 2014, pp. P51C–3962.

[4] D. D. Arumugam, Y. Gim, E. Heggy, and X. Wu, "Synthetic aperture radar imaging of the interior of comets using time-domain back-projection," *2018 IEEE International Symposium on Antennas and Propagation & USNC/URSI National Radio Science Meeting*, IEEE, 2018, pp. 1795–1796.

[5] W. Kofman, A. Herique, Y. Barbin, J.-P. Barriot, V. Ciarletti, S. Clifford, P. Edenhofer, C. Elachi, C. Eyraud, J.-P. Goutail, *et al.*, "Properties of the 67P/Churyumov-Gerasimenko interior revealed by CONSERT radar," *Science*, Vol. 349, No. 6247, 2015.

[6] A. Hérique, W. Kofman, P. Beck, L. Bonal, I. Buttarazzi, E. Heggy, J. Lasue, A. C. Levasseur-Regourd, E. Quirico, and S. Zine, "Cosmochemical implications of CONSERT permittivity characterization of 67P/CG," *Monthly Notices of the Royal Astronomical Society*, Vol. 462, No. Suppl_1, 2016, pp. S516–S532.

[7] P. Sava and E. Asphaug, "3D radar wavefield tomography of comet interiors," *Advances in Space Research*, Vol. 61, No. 8, 2018, pp. 2198–2213.

[8] M. Takala, P. Bambach, J. Deller, E. Vilenius, M. Wittig, H. Lentz, H. M. Braun, M. Kaasalainen, and S. Pursiainen, "Far-field inversion for the deep interior scanning cubesat," *IEEE Transactions on Aerospace and Electronic Systems*, Vol. 55, No. 4, 2018, pp. 1683–1697.

[9] L.-I. Sorsa, M. Takala, P. Bambach, J. Deller, E. Vilenius, and S. Pursiainen, "Bistatic full-wave radar tomography detects deep interior voids, cracks, and boulders in a rubble-pile asteroid model," *The Astrophysical Journal*, Vol. 872, No. 1, 2019, p. 44.

[10] M. Haynes, I. Fenni, Y. Gim, B. Davidsson, C. Raymond, S. Hernandez, S. Bandyopadhyay, J. Stuart, and R. Karimi, "Small Body Radar Inverse Scattering in Monostatic and Bistatic Geometries," *Lunar and Planetary Science Conference*, No. 2548, 2021, p. 1281.

Table 5. Tesseral and sectoral harmonic coefficients.

$C_{1,1}$	0.00000e+00	$S_{1,1}$	0.00000e+00
$C_{2,1}$	1.00308e-04	$S_{2,1}$	−3.27080e-06
$C_{2,2}$	2.33315e-02	$S_{2,2}$	5.78175e-05
$C_{3,1}$	2.22395e-03	$S_{3,1}$	−9.11091e-04
$C_{3,2}$	−1.11713e-02	$S_{3,2}$	−4.02132e-03
$C_{3,3}$	−1.33765e-02	$S_{3,3}$	5.37805e-04
$C_{4,1}$	−9.63397e-04	$S_{4,1}$	−2.50523e-04
$C_{4,2}$	−2.96538e-04	$S_{4,2}$	3.84016e-04
$C_{4,3}$	6.67901e-04	$S_{4,3}$	1.44232e-03
$C_{4,4}$	7.90365e-04	$S_{4,4}$	4.91018e-04
$C_{5,1}$	−7.80999e-04	$S_{5,1}$	−6.07242e-05
$C_{5,2}$	1.39207e-03	$S_{5,2}$	8.54516e-04
$C_{5,3}$	1.44759e-03	$S_{5,3}$	1.19164e-04
$C_{5,4}$	−8.62361e-04	$S_{5,4}$	−8.04965e-04
$C_{5,5}$	−3.09692e-03	$S_{5,5}$	4.00274e-04
$C_{6,1}$	3.53011e-04	$S_{6,1}$	1.60733e-05
$C_{6,2}$	−3.21481e-04	$S_{6,2}$	−4.42653e-04
$C_{6,3}$	−7.69898e-04	$S_{6,3}$	−3.89296e-04
$C_{6,4}$	1.91304e-04	$S_{6,4}$	4.68603e-04
$C_{6,5}$	6.40741e-04	$S_{6,5}$	7.42827e-04
$C_{6,6}$	−5.41320e-04	$S_{6,6}$	−8.75641e-05
$C_{7,1}$	−6.97169e-05	$S_{7,1}$	−1.05541e-04
$C_{7,2}$	−5.70606e-05	$S_{7,2}$	−1.15489e-04
$C_{7,3}$	−1.43889e-05	$S_{7,3}$	9.27033e-05
$C_{7,4}$	−1.73860e-04	$S_{7,4}$	2.18275e-04
$C_{7,5}$	5.12405e-04	$S_{7,5}$	−2.53919e-04
$C_{7,6}$	3.13973e-04	$S_{7,6}$	−4.62986e-04
$C_{7,7}$	−6.49080e-04	$S_{7,7}$	7.26692e-05
$C_{8,1}$	−1.36296e-04	$S_{8,1}$	−9.90542e-05
$C_{8,2}$	−1.67007e-04	$S_{8,2}$	1.74373e-04
$C_{8,3}$	2.18482e-04	$S_{8,3}$	2.11753e-04
$C_{8,4}$	2.08607e-04	$S_{8,4}$	−2.80404e-04
$C_{8,5}$	−2.03853e-04	$S_{8,5}$	−3.15882e-04
$C_{8,6}$	−8.60512e-05	$S_{8,6}$	9.13293e-06
$C_{8,7}$	7.67226e-05	$S_{8,7}$	1.91678e-04
$C_{8,8}$	−1.45247e-04	$S_{8,8}$	−9.91040e-05

[11] W. Kofman, A. Hérique, J.-P. Goutail, T. Hagfors, I. Williams, E. Nielsen, J.-P. Barriot, Y. Barbin, C. Elachi, P. Edenhofer, *et al.*, "The Comet Nucleus Sounding Experiment by Radiowave Transmission (CONSERT): A short description of the instrument and of the commissioning stages," *Space Science Reviews*, Vol. 128, No. 1-4, 2007, pp. 413–432.

[12] P. Michel, M. Küppers, and I. Carnelli, "The Hera mission: European component of the ESA-NASA AIDA mission to a binary asteroid," *cosp*, Vol. 42, 2018, pp. B1–1.

[13] A. Herique, D. Plettemeier, H. Goldberg, and W. Kofman, "JuRa: the Juventas Radar on Hera to fathom Didymoon," *European Planetary Science Congress*, 2020, pp. EPSC2020–595.

[14] J. B. Lundberg and B. E. Schutz, "Recursion formulas of Legendre functions for use with nonsingular geopotential models," *Journal of Guidance Control and Dynamics*, Vol. 11, February 1988, pp. 31–38.

[15] Y. Takahashi and D. Scheeres, "Rapid Characterization of a Small Body via Slow Flybys," AAS/AIAA *Astrodynamics Specialist Conference, AAS 10-244*, Snowbird, UT, 2010.

[16] O. Montenbruck and E. Gill, *Satellite Orbits: Models, Methods and Applications*. Springer, 2005.

[17] M. Brozovic and e. al, "Goldstone and Arecibo radar observations of (99942) Apophis in 2012-2013," *Icarus*, Vol. 300, 2018, pp. 115–128.

[18] M. S. Haynes, I. Fenni, Y. Gim, W. Kofman, and A. Herique, "Angular and Radial Sampling Criteria for Monostatic and Bistatic Radar Tomography of Solar System Small Bodies," *Advances in Space Research*, 2021.

[19] B. D. Tapley, B. E. Schutz, and G. H. Born, *Statistical Orbit Determination*. Elsevier, 2004.